Journal of
Materials Chemistry C

Accepted Manuscript

This article can be cited before page numbers have been issued, to do this please use: I. Golvano-Escobal, B. Özkale, S. Suriñach, D. Baro, T. Drobovolska, I. Krastev, S. Pané, J. Sort and E. Pellicer, *J. Mater. Chem. C*, 2014, DOI: 10.1039/C4TC01316F.

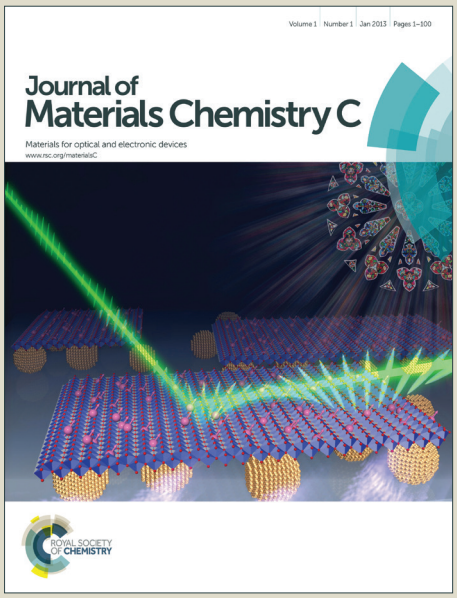

ROYAL SOCIETY OF CHEMISTRY

www.rsc.org/materialsC

View Article Online
DOI: 10.1039/C4TC01316F

Self-organized spatio-temporal micropatterning in ferromagnetic Co-In films

Irati Golvano-Escobal[1], *Berna Özkale*[2], *Santiago Suriñach*[1], *Maria Dolors Baró*[1], *Tsvetina Dobrovolska*[3], *Ivan Krastev*[3], *Salvador Pané*[ξ,2], *Jordi Sort*[*,4] *and Eva Pellicer*[¥,1]

[1]Departament de Física, Universitat Autònoma de Barcelona, E-08193 Bellaterra, Spain.

[2]Institute of Robotics and Intelligent Systems (IRIS), ETH Zürich, CH-8092 Zürich, Switzerland.

[3]R. Kaischew Institute of Physical Chemistry, Bulgarian Academy of Sciences, Sofia, Bulgaria.

[4]Institució Catalana de Recerca i Estudis Avançats (ICREA) and Departament de Física, Universitat Autònoma de Barcelona, E-08193 Bellaterra, Spain.

E-mail:

vidalp@ethz.ch

Jordi.Sort@uab.cat

Eva.Pellicer@uab.cat

Keywords: Co-In, electrodeposition, spatio-temporal organization, magnetic patterning.

View Article Online
DOI: 10.1039/C4TC01316F

Abstract

Cobalt-indium (Co-In) heterogeneous films, featuring spatio-temporal patterns, have been electrodeposited in a chloride-citrate electrolyte. The Co content can be tuned from 25 at% to 90 at% by varying the applied current density between –10 and –30 mA cm^{-2}. The spatio-temporal patterns consist of alternated dark and bright belts, which define micron-sized waves, targets and spirals. Cross-section images indicate a layer-by-layer growth. Several crystallographic phases (hexagonal close-packed Co, face-centered cubic Co, tetragonal In and tetragonal $CoIn_3$) are identified in the corresponding X-ray diffractograms. The films combine large hardness with relatively large Young's modulus and exhibit a soft-magnetic behaviour with tunable saturation magnetisation and coercivity (H_C) values, mostly depending on the Co content and the effective magnetic anisotropy. The film with 90 at% Co shows the highest in-plane H_C (275 Oe) and a squareness ratio close to 1. Magnetic force microscopy observations reveal that the self-patterning is not only topographic but also magnetic. These results demonstrate that electrodeposition of spatio-temporal structures is a simple method to grow magnetically-patterned films, over large areas, in a rapid and inexpensive way. This procedure is highly attractive for the implementation of new types of magnetic sensors, encoding magnetic stripes or even magnetic recording media.

1. Introduction

Spontaneous formation of self-organized spatio-temporal patterns is a phenomenon related to chaos (i.e., fluid instabilities or chemical instabilities) that occurs in dynamic non-linear open systems that are far from equilibrium.[1] Examples of such patterns can be either found in nature (e.g., in the atmosphere and the oceans, in the skin of some animals like the zebra or some fish, in atrial fibrillation, etc.) or they can be experimentally generated in the laboratory,

View Article Online
DOI: 10.1039/C4TC01316F

such as in nanomechanical oscillators or in reaction-diffusion chemical reactions that occur in some immiscible systems (e.g., phase separation, eutectic solidification, etc.). Although linear stability analysis can give some basic understanding of the origin of the pattern formation and the basic length scales, non-linearity remains a fundamental ingredient in order to adequately describe the experimental observations, thus making the problem much more complex and not fully resolved yet.[2,3] Nonetheless, studies aimed at unravelling the mechanisms governing spatio-temporal chaos in dynamic systems remain of utmost importance since more knowledge in the field could allow a better prediction of the nucleation and propagation paths for tornadoes and hurricanes, tectonic motion, the overall evolution of Earth's climate or the transition from normal to arrhythmic heartbeat, amongst others. Directional growth or solidification, in some materials, is also important in terms of the resulting physico-chemical properties. Some eutectic alloys exhibit, for example, outstanding mechanical hardness and have been proposed as ideal heat-transfer materials or as die molds for patterning applications.

The emergence of spatio-temporal patterns can be due to a flux of energy or a flux of matter, e.g. originated from the existence of externally imposed temperature variations (e.g., convection), or by the flow of fluids or chemicals in a reactor. The formation of spatio-temporal structures during electrodeposition was first observed in some Ag alloys (e.g. Ag-Bi, Ag-Cd, Ag-In, Ag-Sb) and attracted the interest of researchers from both experimental and theoretical viewpoints.[4–8] Recently, pattern formation during the electrodeposition of non-Ag based alloys, like Co-In and Ni-P-W-Bi has been demonstrated, hence opening the possibility for additional functionalities (e.g., magnetic) to the previous Ag-based alloys.[9,10] The underlying mechanism for the formation of the spatio-temporal structures is not yet clear and several factors are thought to contribute to the phenomenon, with small differences depending on the system under consideration:[10]

View Article Online
DOI: 10.1039/C4TC01316F

(*i*) the electrolyte hydrodynamic conditions, meaning that the flow along the electrode surface seems to be a necessary condition for pattern formation;

(*ii*) the overpotential, since a threshold value is required for pattern formation. In addition, overpotential has been correlated with the switching among different types of patterns (labyrinths, waves, targets, spirals, broken spirals and mixed patterns);

(*iii*) the ability to self-organize during the growth of multi-phase alloys where a spatial separation of the phases takes place. This has been reported to be one of the key reasons for pattern formation in Co-In electrodeposition;

(*iv*) the kinetic variables, the bath composition (e.g. the counter ion) and the appearance of Turing instabilities in reaction-diffusion systems when the diffusion constants of the different components are quite different from each other.[11]

Bozzini et al. have recently reviewed the literature dealing with pattern formation in alloy electrodeposition and proposed a very innovative and flexible mathematical model to explain the formation of the different types of spatio-temporal structures.[10] Compared to classical models based on systems of reaction-diffusion equations for chemical species, Bozzini's model goes one step further and includes an electrochemical source term to account for adsorbate-induced effects on the kinetic parameters of the electrodeposition process. In such a way, the coupling between surface morphology and surface composition is considered.

Compared to the Ag alloys series, the electrodeposition of Co-In alloys has been much less explored and most of the work has been conducted by Krastev's group. Pattern formation under both stagnant and high speed electrodeposition from electrolytes containing sulphate metal salts and di-ammonium hydrogen citrate at pH around 3 has been established.[9,12] Typically, the ordered spatio-temporal structures form at sufficiently negative current densities (large Co contents).

View Article Online
DOI: 10.1039/C4TC01316F

It cannot be denied that the formation of spatio-temporal structures in alloy electrodeposition is a fascinating phenomenon that deserves investigation. However, the usefulness of growing coatings featuring such patterning, inevitably relies on the ability to find out chemical or physical properties that can certainly benefit from the self-organized structures. In this sense, the study of the physical properties of these self-patterned coatings should turn the corner towards a potential technological application. To the best of our knowledge, the physical properties of Co-In coatings featuring spatio-temporal structures have not been explored. Indium is a very ductile element and has a very low melting point (156.60 °C). For this reason, it has been extensively used in lead-free solders.[13] Indium metal is also employed as a thermal interface material in the electronic industry[14] and in CIS/GICS solar cells. For the latter application, the fabrication of $CuInS_2$ and $Cu(InGa)Se_2$ semiconductor compounds by electrodeposition of In metal on Cu followed by sulfurization or selenization has already been reported.[15] From the magnetic point of view, it has been described that the addition of indium in arc-melted and post-annealed $PrCo_5$ magnets causes an increase of coercivity, H_C, likely due to the formation of the $Pr_3Co_9In_2$ phase.[16] Likewise, addition of Co into InAs, InSb or In_2O_3 has been shown to be a very suitable strategy towards the development of diluted magnetic semiconductors with potential applications in spintronics.[17]

In this work, Co-In films have been electrodeposited from a simple aqueous electrolyte containing chloride metal salts and sodium citrate under stagnant conditions at different current densities. The morphology, composition and crystallographic structure of the galvanostatic deposits obtained on Au/Ti/Si substrates have been systematically studied. According to its phase diagram, In and Co are immiscible in both solid and liquid states.[18] Hence, the formation of multi-phase coatings is anticipated. Energy dispersive X-ray (EDX) mapping analyses of the Co-In films have been conducted in order to explore the chemical composition of the spatio-temporal patterns. Finally, the mechanical and magnetic properties

View Article Online
DOI: 10.1039/C4TC01316F

of the Co-In films have been studied in detail and the data obtained has been correlated with the composition and microstructure of the deposits. The Co-In system is unique in the sense that it is the only binary alloy to simultaneously exhibit ferromagnetic properties with the ability to form spatio-temporal patterns during electrodeposition. This appealing combination of properties is confirmed by magnetic force microscopy observations, which reveal that the films do exhibit 'magnetic micropatterning' linked to the topographical self-organization.

2. Experimental section

Synthesis: Electrochemical experiments were conducted in a three-electrode cell connected to a PGSTAT302N Autolab potenciostat/galvanostat (Ecochemie). A double junction Ag|AgCl (E=+0.210V/SHE) reference electrode (Metrohm AG) was used with 3M KCl inner solution and 1M NaCl outer solution. A platinum sheet served as a counter electrode. A vitreous carbon cylindrical rod with $\pi \bullet 10^{-2}$ cm^2 surface area was used as working electrode (WE) for cyclic voltammetry (CV) studies, whereas silicon (111) substrates with e-beam evaporated Ti (100 nm)/Au (125 nm) adhesion/seed layers were used as WE for both CV studies and deposit growth. The working area of Au/Ti/Si substrates was 5 x 5 mm^2.

In CV studies, three different electrolytes were used: In bath containing 0.30 M $InCl_3$ + 0.05 M $C_6H_5Na_3O_7 \cdot 2H_2O$ + 0.1 M KCl, Co bath containing 0.30 M $CoCl_2$ + 0.05 M $C_6H_5Na_3O_7 \cdot 2H_2O$ + 0.1 M KCl and Co-In bath containing 0.05 M $InCl_3$ + 0.25 M $CoCl_2$ + 0.05 M $C_6H_5Na_3O_7 \cdot 2H_2O$ + 0.1 M KCl. The pH of Co-In electrolyte was left at its unadjusted value (3.1) and the pH of the In and Co baths were adjusted to pH 3.1 by adding NaOH and HCl, respectively. The potential was scanned from 0 V toward different cathodic limits at a scan rate of 50 mV s^{-1}.

View Article Online
DOI: 10.1039/C4TC01316F

Analytical grade reagents and Milipore MilliQ water (MQ-water) were used to prepare the electrolytes. The electrolytic volume was 100 ml. Before each experiment, the electrolyte was de-aerated with nitrogen gas for 10 minutes through a glass purge pipe that provided a vigorous stream of nitrogen. Prior to deposition, the Au seed-layer was first degreased with acetone followed by isopropyl alcohol and MQ-water. Deposition was conducted galvanostatically at 25 ºC. The electrical charge was adjusted across all depositions to 20 C cm^{-2} except for the study of the time-dependent spatio-temporal evolution. After deposition, the films were thoroughly rinsed in water and stored in air.

Characterization: The morphology and the composition of the films were characterized with a Zeiss Merlin field emission scanning electron microscope (FE-SEM) equipped with an energy dispersive X-ray (EDX) detector. Two replicas per condition were analysed. The structure of the films was determined by X-ray diffraction (XRD) on a Philips X'Pert Diffractometer in Bragg-Brentano geometry using Cu Kα radiation (note that both wavelengths $\lambda(K_{\alpha1})$ = 1.5406 Å and $\lambda(K_{\alpha2})$ = 1.5443 Å were used in intensity proportion of $I(K_{\alpha2})=I(K_{\alpha1})$ = 0.5) in the 25º-125º 2θ range (0.03º step size and 10 s holding time).

The mechanical properties of the Co-In films were evaluated by nanoindentation operating in the load control mode using the Ultra-Micro-Indentation System (UMIS) device from Fisher-Cripps laboratories equipped with a Berkovich pyramid-shaped diamond tip. The load-unload curves were taken on the films applying a maximum force of 5 mN. The value of the maximum applied force was chosen to ensure that the maximum penetration depth during the tests was kept below one tenth of the overall thin film thickness. This is considered a necessary condition to avoid any influence from the substrate on the measured mechanical properties.[19] Hardness (H) and reduced elastic modulus (E_r) values were obtained applying the method of Oliver and Pharr.[20] Finally, the elastic recovery was evaluated as the ratio between the elastic and the total (plastic + elastic) energies during nanoindentation, W_e/W_t.

View Article Online
DOI: 10.1039/C4TC01316F

These energies were calculated from the nanoindentation experiments as the areas between the unloading curve and the displacement axis (W_e) and between the loading curve and displacement axis (W_t).[19]

The room temperature magnetic properties were measured using a vibrating sample magnetometer (VSM) from Oxford Instruments. Hysteresis loops were recorded under a maximum applied field of 700Oe applied along the parallel and perpendicular-to-plane directions. Atomic and magnetic force microscopy (AFM/MFM) images were acquired using Dual Scope C-26 system from Danish Micro Engineering. The MFM maps were taken at a tip lift height of 50 nm.

3. Results

3.1. Cyclic voltammetry study

Cyclic voltammetries (CV) recorded from In, Co and Co-In electrolytes on vitreous carbon electrode are shown in Figure 1a. A moderate increase of the reduction current is observed in the In bath (curve *1*) from –0.80 V. In the anodic scan, a double-peak is recorded between –0.4 and –0.6 V. This double-peak corresponds to the oxidation of In-containing species formed on the substrate during the cathodic sweep rather than the oxidation of adsorbed H_2 bubbles arising from the reduction of H^+ ions. When a vigorous stream of Ar gas is provided to the electrolyte during the cathodic scan, the oxidation peak current does not decrease, which otherwise would be observed if most of the reduction current passing through the working electrode (WE) is used to reduce H^+ ions. In such a case, vigorous agitation removes the freshly adsorbed H_2 bubbles on the WE and the corresponding oxidation current recorded during the anodic scan diminishes. For the Co bath, a sharper increase of the reduction current is observed at around –0.95 V, which corresponds to the onset of Co deposition

View Article Online
DOI: 10.1039/C4TC01316F

(curve *2*). A single oxidation peak centered at –0.1 V is observed in the anodic scan. The CV curve recorded from the Co-In electrolyte (curve *3*) shows similar behaviour to the Co bath in the cathodic scan, although the onset for deposition is slightly delayed. In the anodic scan, a small oxidation peak centered at –0.5 V is recorded, followed by a higher oxidation peak at more positive potentials (–0.06 V). Since the first peak appears in the same position as for In electrolyte, it is conjectured that it can be connected with the oxidation of In-rich species. Likewise, the second anodic peak could be assigned to the oxidation of Co-based species. This suggests that a heterogeneous deposit is being formed on the electrode. Finally, it was observed that the onset of deposition on a Au/Ti/Si substrate is shifted toward more positive potentials as compared to the vitreous carbon electrode although the main features of the CV are maintained (Figure 1b).

According to the CV data, deposits could be in principle formed on the Au/Ti/Si electrode at current densities ranging from –10 mA cm^{-2} to –30 mA cm^{-2} (and higher). It was expected that deposits grown at low current densities would contain higher In percentages according to the onset of deposition (–0.95 V for Co electrolyte versus –0.80 V for In electrolyte).

View Article Online
DOI: 10.1039/C4TC01316F

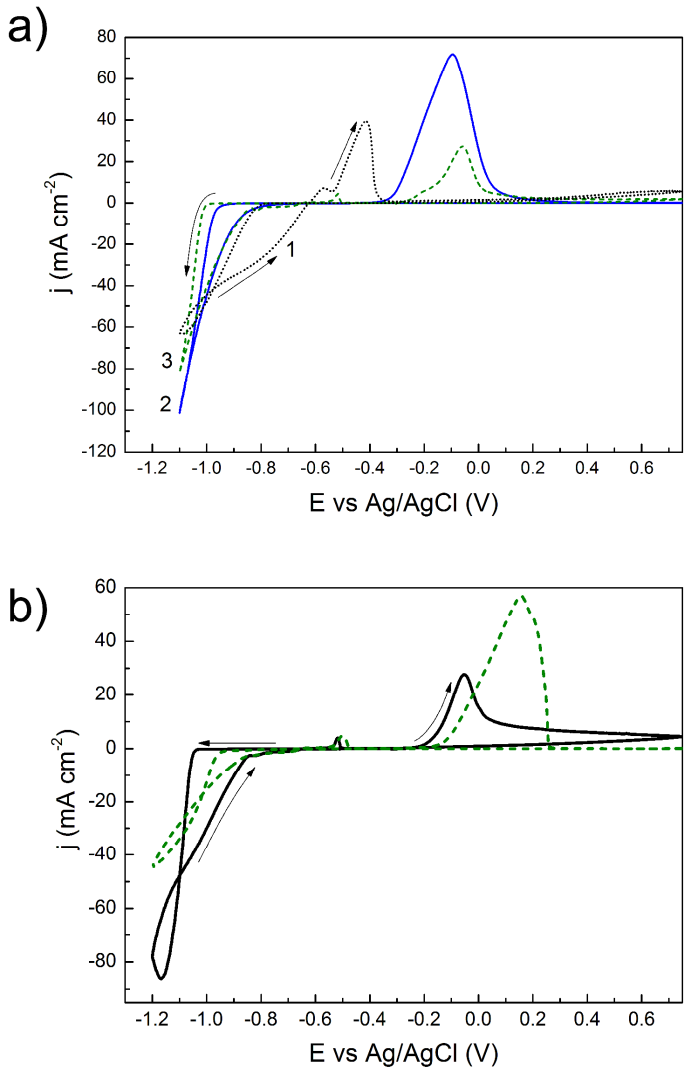

Figure 1. Cyclic voltammetries obtained by polarizing a) a vitreous carbon electrode at cathodic limit of –1.1 V in (1) In bath, (2) Co bath and (3) Co-In bath, b) a vitreous carbon (continuous line) and a Au/Ti/Si substrate (dashed line) at cathodic limit of –1.2 V in Co-In bath. In all cases, scan rate of 50 mV s^{-1} and quiescent conditions were used.

3.2 Morphology and composition of the films

Figure 2 shows the E-t transients for Co-In plated onto Au/Ti/Si substrates at current densities ranging from –10 to –30 mA cm^{-2} and fixed deposition charge (Q = 20 C cm^{-2}) . The curves are characterized by a minimum in the E-t transients that turns into a clear spike with an increase of the absolute value of current density during the first seconds of deposition. This is

View Article Online
DOI: 10.1039/C4TC01316F

followed in all cases by a relaxation of the potential towards a rather stationary value. The value of the stabilized potential decreases as the applied current density is made more negative. The cobalt percentage obtained from EDX analyses drastically increases with a slight increase of the current density from almost pure In films at –10 mA cm^{-2} to 58 at% Co at –12 mA cm^{-2} (Table 1). It is not possible to obtain Co percentages in-between because deposits become rapidly enriched in Co soon after cobalt discharge is allowed. Co percentage rises up to 90 at% with further increase of the current density to –30 mA cm^{-2}.

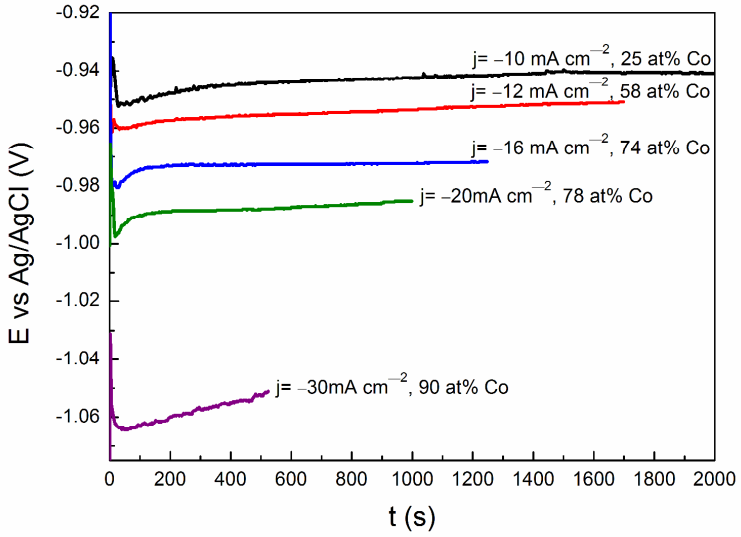

Figure 2. Representative E-t transients for Co-In deposition onto Au/Ti/Si substrates at the indicated current densities. The corresponding average cobalt content in the films is also specified.

Table 1. Values of applied current density (–j), stabilized potential ($-E_S$) of the E-t curve and corresponding Co percentage in the films (mean value ± standard deviation).

–j (mA cm^{-2})	$-E_S$ (V)	at% Co
10	0.94	25*
12	0.95	58 ± 3
16	0.97	74 ± 1
20	0.98	78 ± 1
30	1.05	90 ± 2

*Not homogeneous film composed of large areas with In content approaching 100% and smaller areas showing spatio-temporal organization with ca. 50 at% Co.

View Article Online
DOI: 10.1039/C4TC01316F

With the naked eye, all Co-In deposits show slightly metallic luster appearance and are grey in colour except the coating at –10 mA cm^{-2} that is whitish. Good adhesion to the substrate is observed for nearly all current densities. Incipient peel-off is seen at the edges in films produced at a current density of –30 mA cm^{-2}. Hence, more negative current densities were not considered since film detachment extended across the entire sample/substrate interface. Thick films (10 ± 2 μm) are obtained in all conditions (i.e. for deposition times ranging from 9 min to 33 min).

The occurrence of spatio-temporal structures was already noticed at the optical microscope (not shown). FE-SEM images of the morphology of Co-In films are shown in Figure 3. The spatio-temporal structures are already observed at the lowest current density applied (Figure 3a and 3b). However, in this case, the patterns do not spread all over the substrate but are visible only in some areas of the coating. At current densities of –12 mA cm^{-2} and higher, the spatio-temporal patterns are observed all over the film (Figure 3c-f), and the corresponding deposits feature a mixture of waves, concentric rings (also termed "target patterns") and spirals of variable sizes. No apparent trend between the size of these patterns and the applied current density was seen. EDX analysis revealed that the brighter and darker belts defined by such patterns contained different amounts of Co and In, hence confirming the heterogeneity in composition of the films. EDX-point analyses reveal that the dark belts are typically richer in Co compared to the bright belts by about 30 at% in the case of the film deposited at –10 mA cm^{-2} and about 10 at% for the rest of the films. Since the spatial resolution of the EDX is limited by the interaction volume (X-rays are able to escape not only close to the surface but basically from the whole interaction volume), it is reasonable to assume that the difference in the Co amount at the utmost part of the coating is underestimated.

View Article Online
DOI: 10.1039/C4TC01316F

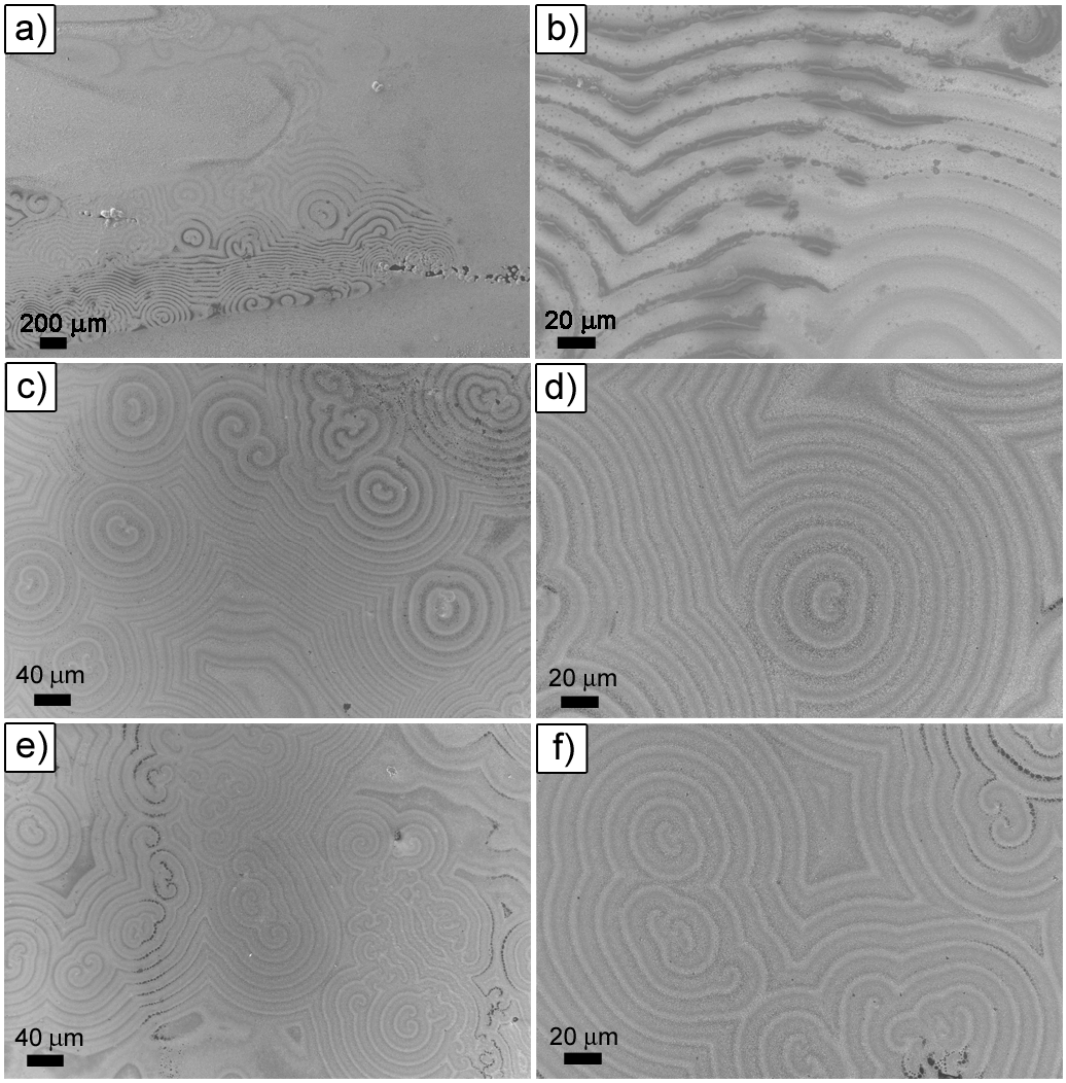

Figure 3. FE-SEM images of Co-In thin films obtained at: a-b) j= –10 mA cm^{-2} (25 at% Co), c-d) j= –12 mA cm^{-2} (58 at% Co) and e-f) j= –20 mA cm^{-2} (78 at% Co).

At higher magnification, sand-like grain morphology is seen all over the film (Figure 4a) except for the sample deposited at –10 mA cm^{-2}. For this sample, the sand-like morphology is also observed in the areas where the spatio-temporal patterns are formed but the rest of the coating features an island-like morphology (Figure 4b) that resembles a Stranski-Krastanov growth mode.[14] In fact, while the Co content is 25 at% on average, the film is not homogeneous in composition. The regions showing spatio-temporal patterns have large Co

View Article Online
DOI: 10.1039/C4TC01316F

contents (~50 at%) whereas the regions without spatio-temporal patterns are made of almost pure In.

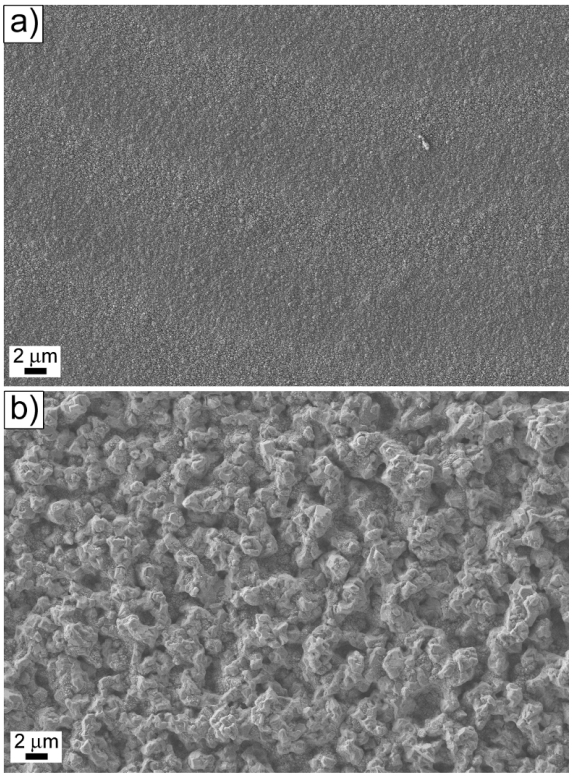

Figure 4. High magnification FE-SEM images of Co-In thin films obtained at: a) j= –30 mA cm^{-2} and b) j= –10 mA cm^{-2} (taken at the region without spatio-temporal patterns).

Figure 5 shows the molar fraction x_i of Co^{2+} and In^{3+} species as a function of pH in the electrolyte. The mole fractions were calculated using MEDUSA® software[21] for all of the bath compounds. The ionic strength was set iteratively by the program. Around pH = 3.0, the most predominant species of Co^{2+} are in form of aquacomplexes (Figure 5a). The molar fraction of cobalt(II) chloride and citrate complexes only represent together x = 0.2 of all the cobalt species. Hydroxocomplexes of Co^{2+} are almost negligible within the pH window hereby considered. On the other hand, In^{3+} is mostly complexed by chlorides (Figure 5b). The

View Article Online
DOI: 10.1039/C4TC01316F

formation of In^{3+} citrate complexes is not considered since there is not available data.[12] Hence, the formation of these species are not considered in this discussion.

The standard electrochemical potentials $E^0_{M^{z+}/M}$ for Co^{2+} and In^{3+} are respectively – 0.28 V and – 0.34 V. At very low current densities, indium plates out preferentially respect to cobalt.[22] This fact seems counterintuitive if one considers the electrochemical potential and the fact that In is mostly complexed by chlorides, while water molecules mostly coordinate Co. However, a work by Bessone and co-workers shows that chlorides facilitate the reduction of In^{3+}.[23] At acidic pHs, the presence of a high positive electrostatic barrier of H^+ near the cathode obstructs the access of positively charged species to the electrode. The high positive charge of In^{3+} is compensated by chloride anions, while Co^{2+} keeps its charge because mainly exists as an aquacomplex. Therefore, it seems reasonable to suppose that deposits are richer in indium at low current densities. When increasing the current density, the deposition process changes drastically leading to films with high cobalt content (Figure 2 and Table 1). This effect could be related to the formation of hydroxocomplexes at the cathode neighbourhood due to hydrogen evolution. Cobalt(II) hydroxocomplexes are readily adsorbed on the cathode and, hence, its reduction is enhanced.

View Article Online
DOI: 10.1039/C4TC01316F

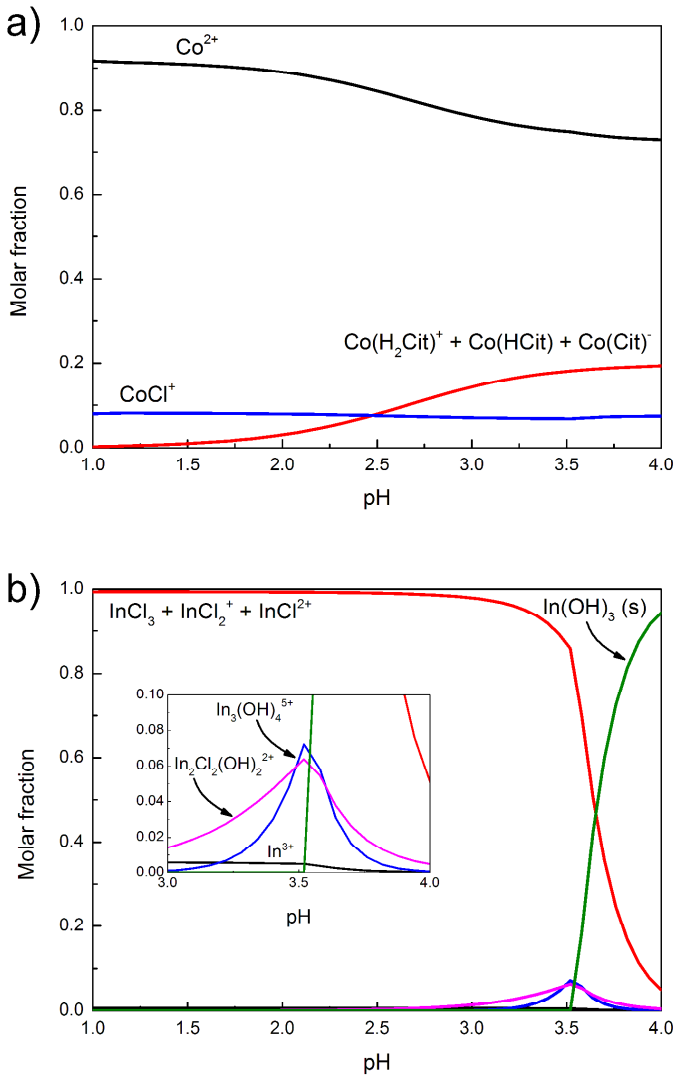

Figure 5. Mole fraction diagrams of a) Co^{2+} and b) In^{3+} species as a function of pH in the electrolyte. The mole fractions were calculated using MEDUSA®. In order to simplify the diagrams, the sum of the mole fractions of the Co^{2+} citrates and the sum of the rest of In^{3+} compounds are represented instead of showing each separately.

3.3 Structural characterization

The structural characteristics of the films obtained through the E-t curves shown in Figure 2 were studied by XRD (Figure 6). Apart from some narrow reflections coming from the substrate (Si and Au seed-layer), all the patterns feature a collection of peaks arising from the electrodeposited films themselves. The diffractograms show reflections that can be assigned

View Article Online
DOI: 10.1039/C4TC01316F

to tetragonal In (PCPDF 05-0642), tetragonal $CoIn_3$ (PCPDF 41-0880), face-centered cubic (fcc) Co and hexagonal-close packed (hcp) Co. As expected, the relative intensity of the In phase peaks decreases as the amount of Co in the films increases. Moreover, no shift of fcc- and hcp-Co peaks toward lower 2θ angles is noticed, indicating that eventual dissolution of In in the Co lattice does not take place (which is in agreement with the very limited solubility of In in Co, the existence of a miscibility gap in this system as reported long ago by Koster and Horn.[24] The coexistence of tetragonal In, fcc-Co and hcp-Co phases clearly demonstrates that a solid solution is not formed but rather separate deposition of Co and In elements (together with intermetallic $CoIn_3$) takes place, instead, during electrodeposition. Nevertheless, the calculated equilibrium phase diagram of the Co+In system establishes the coexistence of hcp-Co and $CoIn_2$ phases at room temperature for Co percentages ≥ 33.3 at%.[18] Interestingly, the monoclinic $CoIn_2$ phase is not detected in our diffractograms, but only the ordered tetragonal $CoGa_3$-type $CoIn_3$ forms, in concordance with a previous work on the electrodeposition of Co-In.[12] It has been claimed that $CoIn_3$ is one of the phases forming the spatio-temporal patterns.[25] A hump at 2θ angles between 40º and 55º overlapped with the reflections is distinguished. This indicates the existence of an additional fraction of amorphous-like contribution, whose relative volume increases with the Co content. Moreover, the full with at half maximum (FWHM) of the fcc-Co, hcp-Co and $CoIn_3$ peaks is larger than for pure In peaks, which suggests that the size of the latter is larger. To further confirm this observation, the Scherrer's formula has been applied to (101) In, (111) fcc-Co and (112) $CoIn_3$ reflections, to obtain a rough estimation of their crystallite sizes (Table 2 and Table S1). These reflections were selected so that they are univocally assigned to only one phase (i.e., no overlapping between phases). While crystallite sizes below 25 nm are generally obtained for fcc-Co or $CoIn_3$, much larger values (around 60 nm) are observed for pure In. It should be pointed out that Co-In coatings electrodeposited from a bath containing $InCl_3$, $CoSO_4$, $(NH_4)_2$HCitrate

View Article Online
DOI: 10.1039/C4TC01316F

and KNaTartrate were also composed of tetragonal In and $CoIn_3$ phases together with hcp-Co.[12] In our work, Co is found as a mixture of fcc, hcp and possibly amorphous phases.

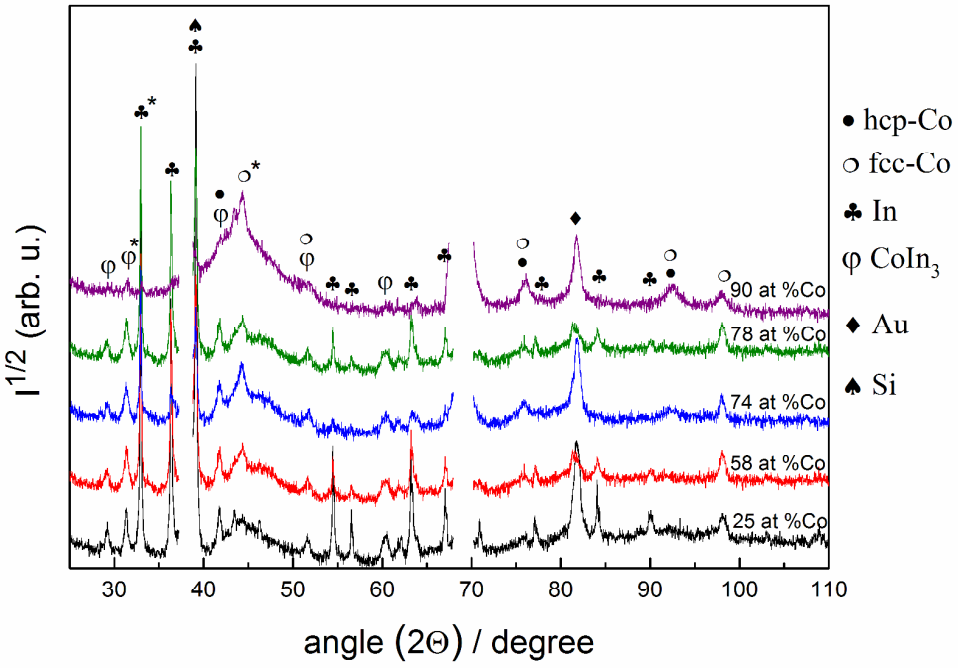

Figure 6. X-ray diffractograms in the 25º-110º 2θ region of Co-In films with different cobalt content deposited on Au/Ti/Si (111) substrates. Breaks in data around 37º and 69º were applied to avoid the most intense reflections from Au and Si, respectively, of the substrate. * Peaks used in Table 2 for FWHM and <D> analysis.

An explanation based on crystallographic considerations has been proposed to account for the spatio-temporal organization in some binary systems like Ag-In, Ag-Sb and Ag-Cd.[25] For example, the XRD patterns of spatio-temporal Ag-In coatings show the existence of fcc Ag and hexagonal $InAg_3$ phases. The similarity between the densely packed (111) plane of the fcc phase and the (0001) plane of the hexagonal $InAg_3$ is thought to contribute to the easy local transition from phase to phase during electrodeposition.[25,26] Likewise, the diffractograms of Ag-Cd films with 80 wt% Cd featuring spatio-temporal patterns evidence that the films are highly textured. The coatings are made of highly oriented hexagonal Cd-

View Article Online
DOI: 10.1039/C4TC01316F

rich ($Ag_{1.05}Cd_{3.95}$) and hexagonal pure Cd phases. The coincidence in the (101) reflection for both phases is believed to contribute to the spatio-temporal organization to some extent.[5,25] However, this explanation does not hold for Co-In system since such similarities cannot be drawn between the fcc or hcp phases of Co and the tetragonal $CoIn_3$.

Table 2. FWHM and corresponding crystallite size (D) calculated using Scherrer's formula for In (101), fcc-Co (111) and $CoIn_3$ (112) peaks for the diffractograms shown in Figure 6.

at% Co	In (101)		fcc-Co (111)		$CoIn_3$ (112)	
	FWHM (º)	⟨D⟩ (nm)	FWHM (º)	⟨D⟩ (nm)	FWHM (º)	⟨D⟩ (nm)
25	0.123	67	--	--	0.325	25
58	0.134	62	0.788	11	0.444	19
74	0.143	58	0.669	13	0.615	13
78	0.132	58	0.891	10	0.634	13
90	--	--	--*	--	0.614	13

*Cannot be precisely determined because it is overlapped with the amorphous background.

3.4 Magnetic behaviour

The magnetic properties of the films were measured by vibrating sample magnetometry (VSM) at room temperature by applying the magnetic field parallel and perpendicular to the film plane (Figure 7). While the films show a ferromagnetic response, the saturation magnetization (M_S) does not linearly scale with the Co percentage. This result corroborates that a Co-In solid solution is not formed, otherwise the sample with 25 at% Co should exhibit a very weak ferromagnetic signal. The non-linear increase of M_S values is due in part to the presence of several phases (In, fcc-Co, hcp-Co and $CoIn_3$), whose relative amounts vary with the applied current density. Magnetic susceptibility measurements of polycrystalline $CoIn_3$

View Article Online
DOI: 10.1039/C4TC01316F

synthesized by reaction at high temperature in tantalum tubes indicate that this compound is weakly paramagnetic at room temperature,[27] while In is diamagnetic. Hence, the observed ferromagnetic response should mainly arise from the pure Co phases.

The films are rather soft-magnetic with in-plane and perpendicular-to-plane coercivities (H_C) and squareness ratios (M_R/M_S) that have different values depending on both the direction of the applied field and the chemical composition (Figure 7 and Table 3). The film with 90 at% Co shows the largest in-plane H_C (275 Oe) and largest in-plane M_R/M_S (virtually 1, i.e. a square hysteresis loop), much larger than M_R/M_S along the perpendicular-to-plane direction (M_R/M_S = 0.45). Hence, this film exhibits a clear in-plane effective magnetic anisotropy, probably dominated by the shape anisotropy (i.e., planar contribution). This shape anisotropy could be due, at least in part, to the formation of the planar spatio-temporal patterns. Interestingly, the values of M_R/M_S along the in-plane direction are reduced in films with lower Co contents, although they remain larger than for measurements along the perpendicular-to-film direction (see Table 3). The in-plane effective magnetic anisotropy is reduced in these films, probably because the ferromagnetic regions (e.g., hcp-Co or fcc-Co) become less interconnected between them and the shape anisotropy arising from the planar geometry of the films is reduced to some extent.

View Article Online
DOI: 10.1039/C4TC01316F

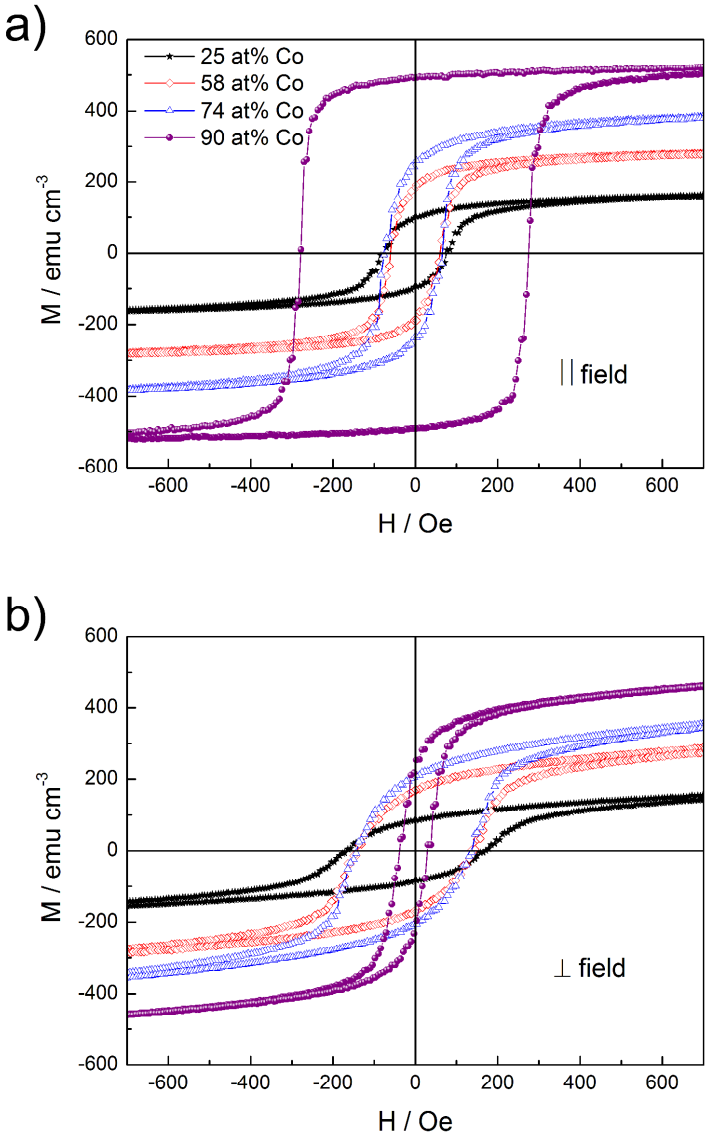

Figure 7. Room-temperature hysteresis loops measured by VSM applying the magnetic field along (a) the in-plane direction and (b) perpendicular-to-plane direction.

The coercivity along in-plane direction is also reduced when the cobalt content is decreased from 90 at% to 74 at% (H_C = 65 Oe) and 58 at% (H_C = 60 Oe). This is mainly due to the loss of magnetic shape anisotropy in the film plane, which in turn is related to an increase of the coercivity with the decrease of the Co content along the perpendicular to film direction. For the sample with 90 at% Co the hysteresis loop along the out-of-plane direction is more difficult to saturate than along the in-plane direction, thus confirming that the easy

View Article Online
DOI: 10.1039/C4TC01316F

magnetization axis lies in plane. For the other films, there is not such a clear easy axis, meaning that there is a competition between shape and magnetocrystalline anisotropies. The out-of-plane H_C of the film with 90 at% Co is 30 Oe, whist higher values (140-170 Oe) apply for the other Co-In films.

Table 3. Saturation magnetization (M_S), squareness ratio (M_R/M_S) and coercivity (H_C) of Co-In films as a function of their average Co percentage. The symbols ∥ and ⊥ mean that the field was applied parallel and perpendicular to the film plane, respectively.

at% Co	M_S [emu cm^{-3}]	M_R / M_S ∥	H_C ∥ [Oe]	M_R / M_S ⊥	H_C ⊥ [Oe]
25	163	0.59	75	0.52	170
58	275	0.68	60	0.61	138
74	387	0.65	65	0.54	136
90	525	0.93	275	0.45	30

Atomic force microscopy (AFM) coupled to magnetic force microscopy (MFM) analysis of the samples was performed to reveal whether the spatio-temporal organization gave rise to any magnetic contrast besides the topological self-patterning. Figure 8 shows the AFM and MFM images for the film deposited at −10 mA cm^{-2}, taken at a region where the spatio-temporal organization occurred. The AFM image displays the typical belts observed by SEM, being the peak-to-valley distance equal to 225 nm. Interestingly, the corresponding MFM image shows a clear magnetic contrast that follows the topographical pattern. This proves that the spatio-temporal patterns do exhibit some kind of inherent 'magnetic micropatterning'. A similar response was observed in corrugated cobalt filaments also made by electrodeposition.[28] The MFM analysis was also performed on other films produced at higher current densities. MFM images also reveal some magnetic contrast, but less pronounced because the films are probably entirely magnetic.

View Article Online
DOI: 10.1039/C4TC01316F

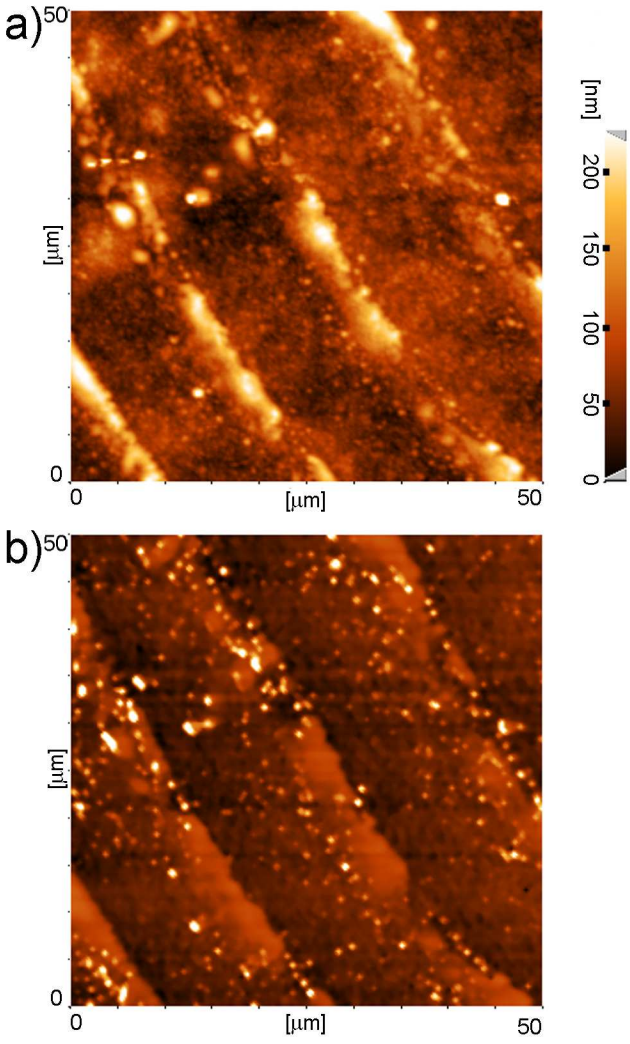

Figure 8. a) AFM and b) MFM images taken on scanned 50 x 50 µm^2 area containing spatio-temporal patterns for the sample deposited at –10mA cm^{-2}.

3.5 Mechanical behaviour

The mechanical properties of the Co-In films were studied by nanoindentation. Figure 9a shows representative loading-unloading curves performed on-top of the films. The curve for the sample with 25 at% Co on average was obtained from an area featuring spatio-temporal patterns (i.e., not on the pattern-free areas which consists of almost pure In). The penetration depth at the end of the loading segment for this film is lager compared to the film with the

View Article Online
DOI: 10.1039/C4TC01316F

highest Co content (90 at%). The values of hardness (H), reduced Young's modulus (E_r) and the H/E_r ratio are listed in Table 4. As expected, both H and E_r are slightly lower for the In-rich sample. Even if the indentation for this sample has been performed on the spatio-temporal patterns where $CoIn_3$ is thought to be the main component, the amount of pure In phase accompanying the $CoIn_3$ is higher. Therefore, the obtained results make sense considering that In metal is recognized as a very ductile element due to its low Young's modulus.[29] In fact, a value of E_r = 3.3 GPa is obtained when the indentation is performed on the free-patterned area made of almost pure In. The film with 90 at% Co shows that largest H (7.00 GPa) and E_r (151.3 Ga). The H/E_r ratio, which provides an indirect estimation of the wear resistance of a coating,[30,31] is kept rather constant among all films. Similarly, the elastic recovery (W_e/W_t) and the ratio between the plastic and the total energy (W_p/W_t) are also similar for all coatings. Figure 9b shows an array of indentations performed on the surface of the Co-In film with 58 at% Co. As it can be seen in the figure, the lateral size of the indents is rather small (smaller than 0.5 μm, see magnified detail of one indentation in the inset). No significant differences are observed in the size of the imprints as most of them do not indent only the dark or bright belts but lay in between.

Table 4. Hardness (H), reduced Young's modulus (E_r) and H/E_r, W_e/W_t and W_p/W_t ratios for the Co-In films with the indicated Co contents.

at% Co	H (GPa)	E_r(GPa)	H/E_r	W_e/W_t	W_p/W_t
25	6.2 ± 1.2	120.6 ± 13.8	0.05 ± 0.01	0.34 ± 0.03	0.66 ± 0.09
58	6.6 ± 1.1	128.4 ± 15.4	0.05 ± 0.01	0.33 ± 0.03	0.66 ± 0.09
74	6.9 ± 1.3	130.8 ± 16.3	0.05 ± 0.01	0.34 ± 0.03	0.66 ± 0.09
90	7.0 ± 1.6	151.3 ± 19.9	0.04 ± 0.01	0.30 ± 0.04	0.69 ± 0.14

View Article Online
DOI: 10.1039/C4TC01316F

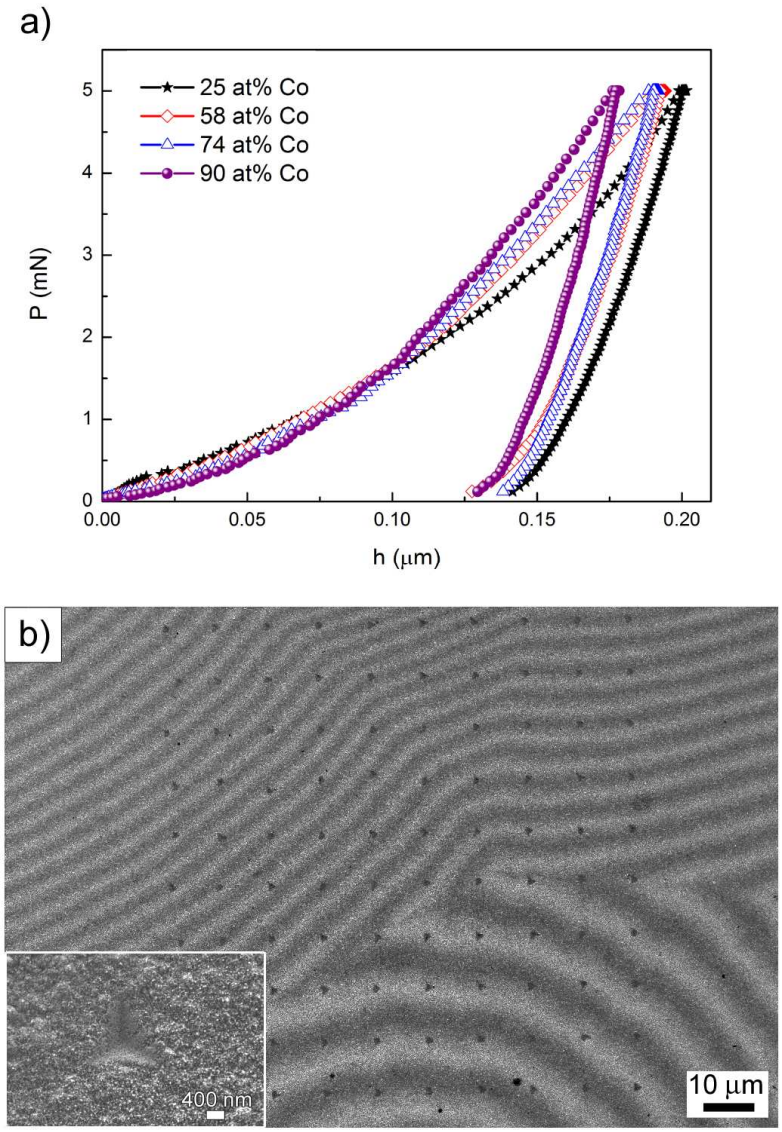

Figure 9. a) Load-unload nanoindentation curves performed on the surface of Co-In films with variable Co content. b) SEM image showing an array of indentations performed on the surface of Co-In film with 58 at% Co. The inset shows a magnified detail of an indent imprint.

3.6 Spatio-temporal patterns evolution with time

View Article Online
DOI: 10.1039/C4TC01316F

To gain a better understanding of the evolution of the spatio-temporal structures as a function of the deposition time (i.e, the thickness), a new series of Co-In films was fabricated at a constant current density of –16 mA cm^{-2} for different deposition times (250 s – 3000 s). Figure 10A shows the E-t curve with dots labelled as (a-d) corresponding to each deposition time together with the average Co percentage. Figure 10B shows secondary electron SEM images (left column) of a spiral together with the corresponding Co, In (and O) elements distribution determined by EDX mapping analysis. The analysis reveals that the local distribution of Co (in red) and In (in green) elements within the spatio-temporal patterns is not homogeneous and that such effect is intensified with the deposition time. On comparing the SEM images of the coatings obtained through points (a-c) as indicated in the E-t curve, with the corresponding element mappings, one can observe that the Co signal is higher in the dark belt of the spiral whereas that of In is higher in the brighter belt. Furthermore, significant amounts of oxygen are detected in the films obtained for longest deposition time (3000 s, point *d* of the E-t curve). The O signal is preferably detected in the In-rich belts, shown as black spots on the SEM image and in violet colour in the corresponding mapping, suggesting incipient formation of oxide/hydroxide species in the In-rich belts of spatio-temporal patterns. Figure 11 shows the XRD patterns of these films obtained at different deposition times. The relative intensity of both In and $CoIn_3$ reflections progressively increase with the deposition time. Concomitantly, the hcp- and fcc-Co reflections diminish in intensity. This result suggests that the volume fraction of In and $CoIn_3$ phases increases with deposit thickness. The time-dependent magnetic and mechanical behaviour of these films is shown in Figure S1 and Table S2, respectively. Figure 12 shows a cross-section image of the thickest film within this series, where a layer-by-layer growth type is evident. Due to the polishing procedure, the layers became separated from each other in some regions of the coating (Figure 12a). The thickness of each layer is roughly around 60 nm (Figure 12b). The distribution of Co and In

View Article Online
DOI: 10.1039/C4TC01316F

elements is kept rather constant throughout deposit thickness (Figure 12c) and within each nanolayer (Figure S2) in spite of using quiescent conditions during electrodeposition.

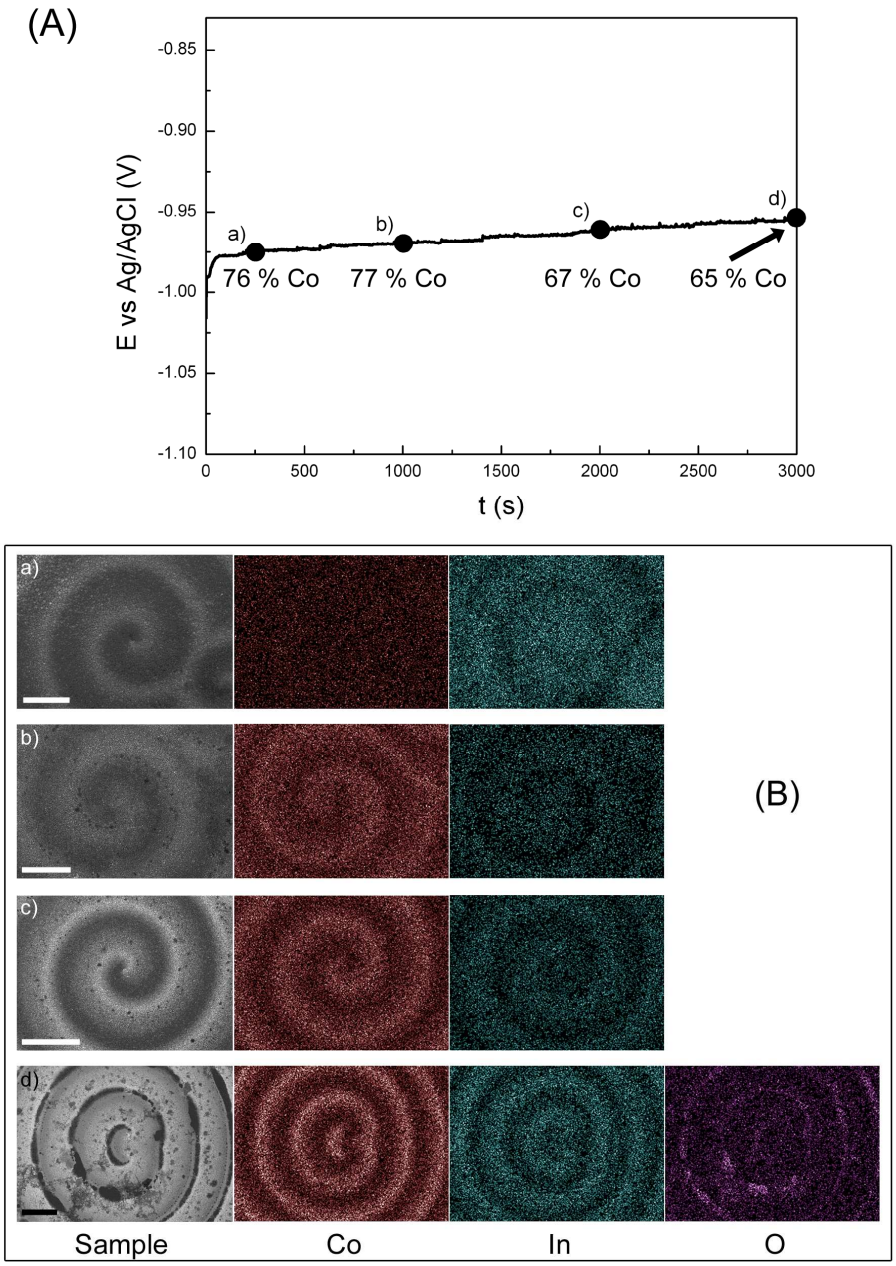

Figure 10. (A) E-t transient for Co-In deposition onto Au/Ti/Si substrate at a constant current density of –16 mA cm^{-2} and different deposition times: a) 250 s, b) 1000 s, c) 2000 s and d) 3000 s. (B) EDX mapping analysis of a region of the coating corresponding to the time-points (a-d) indicated in (A). Scale bars in a) and b) is 10 µm, 20 µm in c) and 30 µm in d).

View Article Online
DOI: 10.1039/C4TC01316F

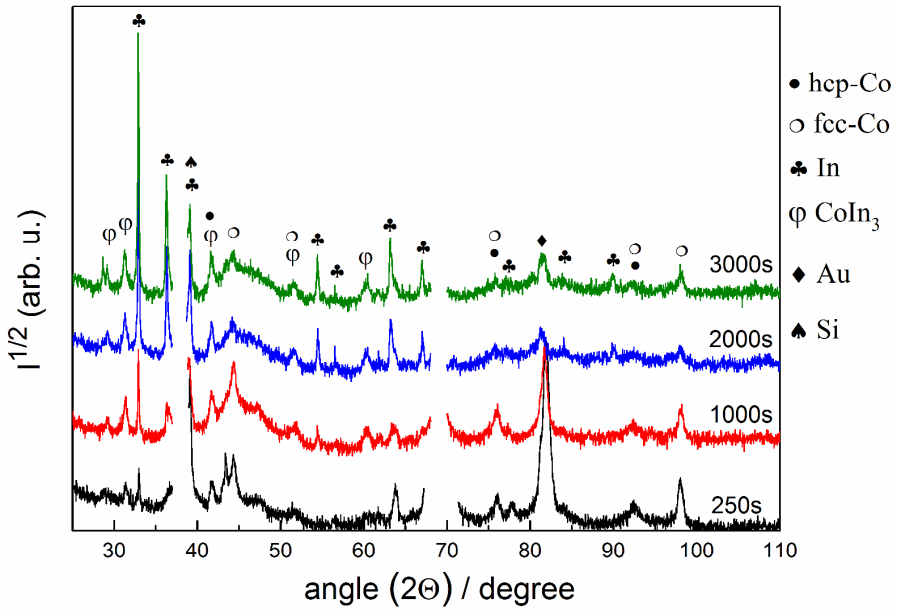

Figure 11. XRD patterns of Co-In films obtained at –16 mA cm^{-2} for deposition times corresponding to the time-points (a-d) indicated in Figure 10(A). Breaks in data around 37º and 69º were applied to avoid the most intense reflections from Au and Si, respectively, of the substrate.

4. Conclusions

Heterogeneous Co-In films featuring spatio-temporal patterns have been electrodeposited by direct current on Au/Ti/Si substrates from a citrate-chloride bath. The applied current densities allow producing either In-rich films (25 at% Co) showing incipient spatio-temporal organization on small areas of the coating or Co-rich films (58-90 at% Co) featuring spatio-temporal patterns on the entire surface. The films are composed of several phases (tetragonal In and $CoIn_3$, fcc-Co and hcp-Co) and exhibit tuneable magnetic and mechanical properties as a function of the relative phase percentages and compositions. The films show soft ferromagnetic behaviour with in-plane coercivities between 75 and 275 Oe. Nanoindentation tests reveal that all samples exhibit a combination of large hardness with relatively high Young's modulus. It has been demonstrated by EDX mapping analyses that the dark and

View Article Online
DOI: 10.1039/C4TC01316F

bright belts defined by the spatio-temporal structures are progressively enriched with Co and In, respectively, as the deposition time is increased. The occurrence of self-organization during electrodeposition renders a material featuring both topographical and magnetic micropatterning, which opens new opportunities for Co-In films in magnetic applications such as sensors or encoders.

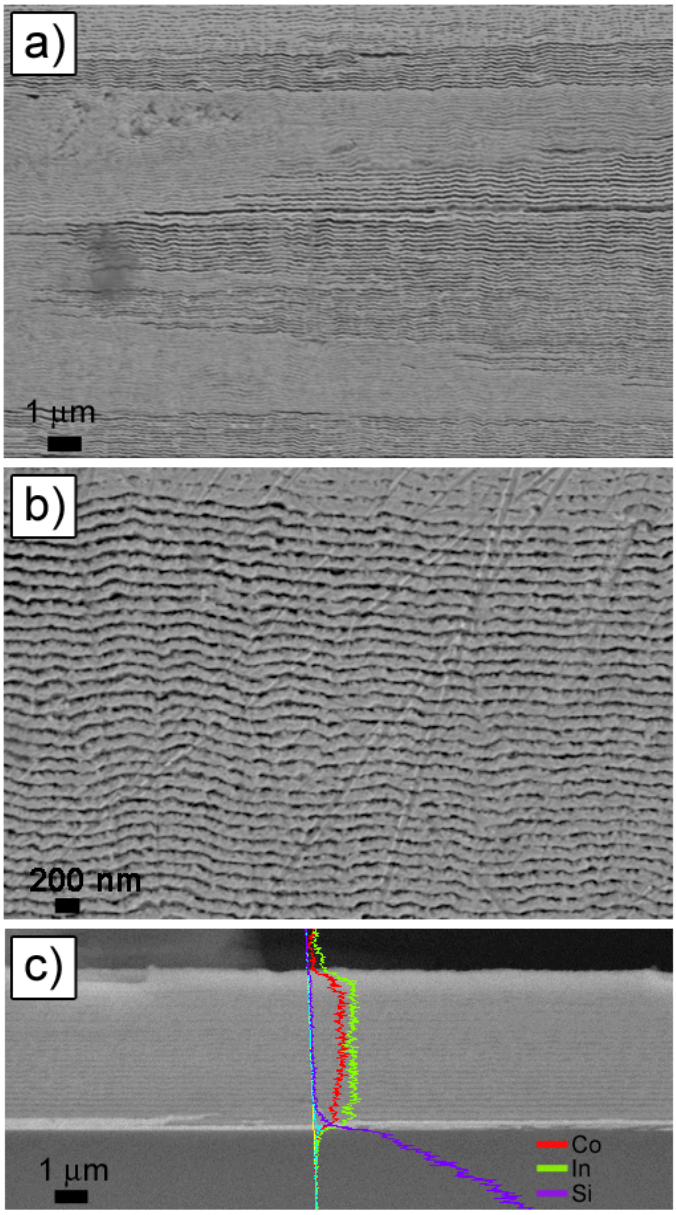

Figure 12. Cross section of Co-In film obtained at –16 mA cm^{-2} for 3000 s deposition time a-b) SEM image, and c) EDX line scan analysis.

View Article Online
DOI: 10.1039/C4TC01316F

Acknowledgements

Funding from the Spanish MINECO (MAT2011-27380-C02-01) and the Catalan DGR (2014-SGR-1015) are acknowledged. M.D.B. acknowledges partial financial support from an ICREA-Academia Award. E.P. thanks MINECO for the 'Ramon y Cajal' contract (RYC-2012-10839).

View Article Online
DOI: 10.1039/C4TC01316F

References

(1) D. A. Egolf, I. V. Melnikov, W. Pesch, R. E. Ecke, *Nature*, 2000, **404**, 733–736.

(2) M. Bestehorn, R. Friedrich, *Phys. Rev. E*, 1999, **59**, 2642–2652.

(3) H. Kitahata, K. Yoshikawa, *J. Phys.: Condens. Matter*, 2005, **17**, S4239–S4248.

(4) I. Krastev, T. Valkova, A. Zielonka, *J. Appl. Electrochem.*, 2004, **34**, 79–85.

(5) Ts. Dobrovolska, D. A. López-Sauri, L. Veleva, I. Krastev, *Electrochim. Acta*, 2012, **79**, 162–169.

(6) Ts. Dobrovolska, L. Veleva, I. Krastev, A. Zielonka, *J. Electrochem. Soc.*, 2005, **152**, C137–C142.

(7) Y. Nagamine, O. Haruta, M. Hara, *Surf. Sci.*, 2005, **575**, 17–28.

(8) I. Kristev, M. Nikolova, *J. Appl. Electrochem.*, 1986, **16**, 875-878.

(9) M. A. Estrella Gutiérrez, Ts. Dobrovolska, D. A. López Sauri, L. Veleva, I. Krastev, *ECS Trans.*, 2011, **36**, 275–281.

(10) B. Bozzini, D. Lacitignola, I. Sgura, J. Sol. State Electrochem., 2013, **17**, 467–479.

(11) A. M. Turing, *Phil. Trans. R. Soc. B.*, 1952, **237**, 37–72.

(12) I. Krastev, Ts. Dobrovolska, U. Lačnjevac, S. Nineva, *J. Sol. State Electrochem.*, 2012, **16**, 3449–3456.

(13) L. J. Turbini and D. Bernier, *Handbook of lead-free solder technology for microelectronic assemblies* (Ed. Karl J. Puttlitz, Kathleen A. Stalte), Marcel Dekker Inc., USA 2004, p. 98.

(14) Q. Huang, K. Reuter, S. Amhed, L. Deligianni, L. T. Romankiw, S. Jaime, P.-P. Grand, V. Charrier, *J. Electrochem. Soc.*, 2011, **158**, D57–D61.

(15) X. C. Tong, *Advanced Materials for Thermal Management of Electronic Packaging*, Springer New York, 2011, 305–371.

(16) A. M. Gabay, G. C. Hadjipanayis, J. Alloy Compd., 2010, **500,** 161–166.

View Article Online
DOI: 10.1039/C4TC01316F

(17) T. Dietl, *Nature Mater.*, 2010, **9**, 965-974.

(18) J. P. Bros, M. Gaune-Escard, D. El Allam, R. Haddad, E. Hayer, *J. Alloy Comp.*, 1996, **233**, 264–271.

(19) A. C. Fisher-Cripps, *Nanoindentation* (Ed: F. F. Ling), Springer, New York, 2004.

(20) W. C. Oliver, G. M. Pharr, *J. Mater. Res.*, 1992, **7**, 1564–1583.

(21) I. Puigdomènech. Medusa software, http://www.kth.se/che/medusa

(22) Y. N. Sadana, A. E. Keskinen, M. Guindon, *Electrodeposition and Surface Treatment*, 1975, **3**, 149–157.

(23) A.G. Muñoz, S. B. Saidman, J. B. Bessone, *J. Electrochem Soc.*, 1999, **146**, 2123–2130.

(24) W. Koster and E. Horn, Z. *Metallkd*., 1952, **43**, 333–334.

(25) I. Krastev, Ts. Dobrovolska, *J. Solid State Electrochem.*, 2013, **17**, 481–488.

(26) T. Dobrovolska, G. Beck, I. Krastev, A. Zielonka, *J. Sol. State Electrochem.*, 2008, **12**, 1461–1467.

(27) R. Pöttgen, R.-D. Hoffmann, G. Kotzyba, *Z. Anorg. Allg. Chem.*, 1998, **624**, 244–250.

(28) X.-P. Huang, Z.-L. Shi, M. Wang, M. Konoto, H.-S. Zhou, G.-B. Ma, D. Wu, R. Peng, N.-B. Ming, *Adv. Mater.*, 2010, **22**, 2711-2716.

(29) H. Ledbetter, N. Sizova, S. Kim, H. Kobayashi, S. Sgobba, L. Parrini, *J. Phys. IV*, 1996, **C8**, 317–318.

(30) A. Leyland, A. Matthews, *Wear*, 2000, **246**, 1–11.

(31) E. Pellicer, A. Varea, S. Pané, B. J. Nelson, E. Menéndez, M. Estrader, S. Suriñach, M. D. Baró, J. Nogués, J. Sort, *Adv. Funct. Mater.*, 2010, **20**, 983–991.